ECS The Electrochemical Society
Advancing solid state & electrochemical science & technology

Analysis of the Polarization in a Li-Ion Battery Cell by Numerical Simulations

View the article online for updates and enhancements.

Analysis of the Polarization in a Li-Ion Battery Cell by Numerical Simulations

Andreas Nyman,* **Tommy Georgios Zavalis,*,z** **Ragna Elger, Mårten Behm,****
and Göran Lindbergh**

Applied Electrochemistry, Department of Chemical Engineering and Technology, School of Chemical Science and Engineering, Royal Institute of Technology KTH, Kungliga Tekniska Högskolan, SE-100 44 Stockholm, Sweden

An experimentally validated model was developed to analyze the polarization of a $LiNi_{0.8}Co_{0.15}Al_{0.05}O_2|1.2$ M $LiPF_6$ in ethylene carbonate (EC):ethyl methyl carbonate (EMC) (3:7)|MAG-10 battery cell during a hybrid pulse power characterization (HPPC) cycle. The analysis was made with a method where the polarization was split up into parts associated with activation of the electrochemical reactions, mass transport of species in the electrolyte and in the solid phase, and inadequate contact between the materials in the electrodes. Each contribution to the polarization was quantified as a snapshot in time and as an average over the HPPC cycle. The polarization during a cycle according to EUCAR was analyzed in detail for state of charge (SOC) 40 and 80. It arose mainly due to the mass transport in the electrolyte, e.g., at SOC 40 it contributed to 43% of the total polarization. In an ISO (International Organization for Standardization)-energy cycle where the current loads are higher and applied for longer times than the EUCAR cycle, the mass transport by diffusion in the electrolyte and in the solid phase of the negative electrode became more significant. The presented method offers the possibility to find a battery cell's optimal operational condition and design.
© 2010 The Electrochemical Society.   [DOI: 10.1149/1.3486161] All rights reserved.

The performance of batteries for hybrid electric vehicles (HEVs) is often evaluated in terms of, e.g., the power and the energy efficiency, as measured in hybrid pulse power characterization (HPPC) tests. During such tests, high discharge and charge currents are applied to the cells at various states of charge (SOCs). The performance is limited by the polarization of the battery cell. For lithium-ion batteries, there is a general consensus that polarization is caused by mass transport limitations in the electrolyte and the solid phase of the electrodes, contact problems between the solid phases, and slow electrochemical reactions.[1] The contribution of each process to the polarization in a battery is dependent on the thermodynamic and kinetic material properties, the battery cell design, and how the cell is charged/discharged. These relations generally become very complex, and to understand and explain the polarization in detail, mathematical modeling can be used.

Mathematical models describing the physical properties of lithium-ion battery cells were first published in the beginning of the 1990s by Newman's group.[2-6] They were based on well-proven electrochemical concepts and satisfied thermodynamic constraints.[7-10] Similar models have been used to describe many other electrochemical systems, e.g.[11-13] Physically based models of lithium-ion battery cells provide results that show the spatial variation in the lithium-ion concentration, electrochemical potential, and reaction rates with time, which are hard to obtain experimentally. The early models were developed for energy-optimized batteries and the models were thus simulated for low current loads. During the past decade, the research focus has turned toward power-optimized batteries. The demands of the models have been shifted to describe the performance during high loads (>5 C) as well.[14-16] This had led to the use of refined descriptions of especially the mass transport in the electrolyte[14] and in the active materials.[17,18] Some examples of such refinements are SOC-dependent properties of the active material related to kinetics and mass transport,[19-21] a size distribution of the active material particles,[17,20] and nonidealities in the electrolyte.[22,23] When the models are refined, the number of parameters that describe the system is consequently increased. This may be an obstacle when simulating because there is a lack of published data for many of these parameters.

In this work, we have chosen to model and simulate a $LiNi_{0.8}Co_{0.15}Al_{0.05}O_2|LiPF_6$, ethylene carbonate (EC):ethyl methyl carbonate (EMC) (3:7)|MAG-10 cell during an HPPC test defined according to EUCAR.[24] This system is interesting from an application point of view and there are data and models available for the description of the electrochemistry of the system. The model is based on the recent electrode characterization by Brown et al.[20,21] and Mellgren et al.[19] and the electrolyte study by Nyman et al.,[23] which is one of the very few complete characterizations of lithium-ion battery electrolytes based on the concentrated electrolyte theory.

When analyzing simulated data, it is common to plot the change in the concentration and/or potential profiles over time.[2-4,6,25-32] The analysis gives an insight in the dynamics of the processes and in possible limitations but it is not sufficient to quantify the importance of the separate processes in terms of polarization. A difficulty facing such quantification arises due to uneven current and concentration distribution in the porous electrodes. To circumvent this, a strategy based on parameter variation has been used.[18,33] A parameter associated with a process was set to a large or small value to negate its effect in the model. The difference between the cell voltages was then attributed to the polarization of the process. However, doing so overestimates the effect of a single process and, thus, the sum of all the polarizations is not equal to the total polarization.

In the present work, a new method is presented that enables both quantification and localization of the polarization in a battery cell. The part of the polarization that arises due to a certain process is calculated directly from the potential and concentration profiles in the cell. The sum of all the parts is therefore equal to the total polarization of the cell. The analysis is based on splitting up the polarization into parts attributed to processes that occur in the cell during operation. In addition, an averaged polarization for the whole test cycle is calculated. Finally the procedure is used to see how the polarization is changed for different charging/discharging conditions and battery designs.

Model Description

A model describing the electrochemical behavior of the battery cell was set up and solved in COMSOL Multiphysics with the parameters presented in Table I. The model constitutes a theoretical basis for the discussion regarding the polarization arising in the cell. Newman at the University of California is accredited for the development of the general mathematical methodology of the full cell model[10,34] and similar models have been published pre-

* Electrochemical Society Student Member.
** Electrochemical Society Active Member.
   z E-mail: zavalis@kth.se

Table I. Model parameters.

Parameter	Value/expression	Source
R	8.314 J mol^{-1} K^{-1}	Physical constant
T	298 K	
F	96,487 A s mol^{-1}	Physical constant
D_S^+	1.109 × 10^{-15} m^2 s^{-1} (SOC 40)	Ref. 20
	1.607 × 10^{-15} m^2 s^{-1} (SOC 80)	
D_S^-	7.477 × 10^{-18} m^2 s^{-1} (SOC 40)	Ref. 21
	4.820 × 10^{-17} m^2 s^{-1} (SOC 80)	
r_p^+	2.49 × 10^{-7} m	Ref. 20
z_p^-	4.48 × 10^{-8} m	Ref. 21
α_a	0.5	Assumed value
α_c	0.5	Assumed value
k_a^+	2.198 × 10^{-11} (SOC 40)	Ref. 20
	1.457 × 10^{-12} (SOC 80)	
k_a^-	2.551 × 10^{-11} (SOC 40)	Ref. 21
	7.070 × 10^{-11} (SOC 80)	
β_L^+	2.928	Ref. 20
β_L^-	2.854	Ref. 21
β_L^S	2.25	Estimated from Ref. 41 and 42
β_{cS}^+	1.5	Ref. 20
β_S^-	1.5	Ref. 21
ε_S^+	0.482	Calculated from manufacturer data
ε_{cS}^+	0.11	Ref. 20
ε_S^-	0.62	Calculated from manufacturer data
ε_L^+	0.29	Ref. 20
ε_L^-	0.31	Ref. 21
ε_L^S	0.40	Estimated from Ref. 42
$V_{m,LiPF_6}$	59 × 10^{-6} m^3 mol^{-1}	Ref. 23
$V_{m,solv}$	87 × 10^{-6} m^3 mol^{-1}	Ref. 23
σ_{cS}^+	91 S m^{-1}	Ref. 21
σ_S^-	100 S m^{-1}	Estimated as a high value
R_{loc}^+	1.582 × 10^3 Ω m^2	Optimized
$R_{contact}$	7.127 × 10^{-4} Ω m^2	Optimized
$c_{S,tot}^+$	33,956 mol m^{-3}	Calculated from nom. spec. capacity in Ref. 21
$c_{S,tot}^-$	31,229 mol m^{-3}	Calculated from nom. spec. capacity in Ref. 21
SOC_0^+	0.566 (SOC 40)	Estimated from Ref. 20
	0.387 (SOC 80)	
SOC_0^-	0.30 (SOC 40)	Ref. 21
	0.58 (SOC 80)	
E_{ref}^+	3.6	Parameter selected to fit Eq. 10
E_{ref}^-	0	Parameter selected to fit Eq. 10
a^+	$3\varepsilon_S^+/r_p^+$	—
a^-	1.1006 × 10^7	Estimated from Ref. 21

viously.[2-4,6,25-32] Even if the full cell model in this study is inspired by these publications, it differs in some details and is therefore described below.

The equations are used to describe the spatial and time-dependent variation in the potential as well as the lithium-ion concentration in the solid and electrolyte phases. The ones associated with the electrolyte and the potentials are solved in 1D for a cross section from the negative to the positive current collector (Fig. 1). The lithium concentration within the active material is resolved for both the spatial variation along the x-direction in Fig. 1 and the depth of the active material particles.

It is assumed that the positive electrode consists of three phases: an electronically conductive phase, an active material phase, and a liquid electrolyte phase. Electrons are transported in the conductive phase between the current collector and the active material. The variation in solid phase potential in the conductive phase (φ_{cS}^+) is described by Ohm's law

$$j_S^+ = -\sigma_{cS}^+(\varepsilon_{cS}^+)^{\beta_{cS}^+}\frac{\partial \varphi_{cS}^+}{\partial x} \quad [1]$$

where j_S^+ is the current density in the solid phase, σ_{cS}^+ is the electronic conductivity, ε_{cS}^+ is the fraction of volume in the electrode that

⇐⇒ Active material negative electrode ■ Negative current collector

◇ Active material positive electrode ▨ Positive current collector
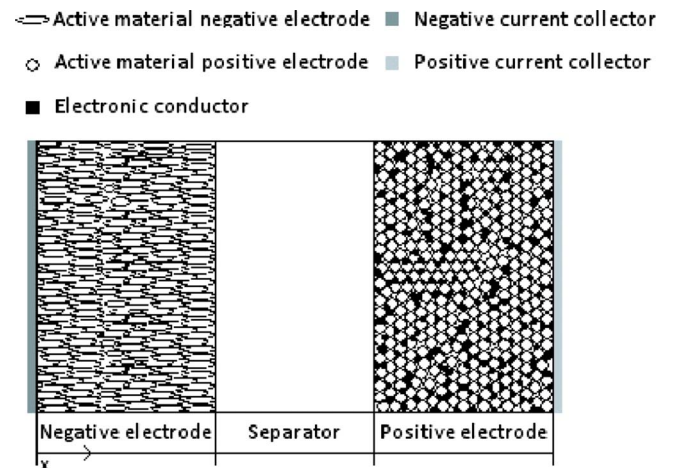
■ Electronic conductor

Figure 1. (Color online) Schematic of the lithium-ion battery cell.

is occupied by the conductive phase, and β_{cS}^+ is Bruggeman's constant for the conductive phase.

A film that hinders the transport of ions has been reported to exist on the surface of the active particles in the positive electrode.[19,20,35] In this work, it is assumed that the lithium ions need to migrate through this film to react electrochemically with the active material and this gives rise to a resistance. Inadequate contact between the electronically conducting phase and the active material phase also leads to a resistance. From a mathematic perspective, these two effects cannot be separated and are therefore modeled as a single local resistance (R_{loc})[6,19,36]

$$\varphi_S^+ = \varphi_{cS}^+ - j_{loc}R_{loc}^+ \quad [2]$$

where φ_S^+ is the active material phase potential and j_{loc} is the local current per active material area. The value of the local resistance is discussed later in the Model Description section.

In the solid phase of the negative electrode, only an active material phase is assumed to exist due to the high electronic conductivity of the graphite. The variation in active material phase potential (φ_S^-) is expressed as Ohm's law[21]

$$j_S^- = -\sigma^-(\varepsilon_S^-)^{\beta_S^-}\frac{\partial \varphi_S^-}{\partial x} \quad [3]$$

where j_S^- is the current density in the solid phase, σ_S^- is the electronic conductivity, ε_S^- is the fraction of volume in the electrode that is occupied by the conductive phase, and β_S^- is Bruggeman's constant.

In the active material, lithium ions are assumed to be transported by diffusion. This is consistent with previous models of the same electrode.[21] The electrodes consist of differently shaped and sized particles, influencing the lithium transport rate. However, in this study the particle size distributions in both electrodes are neglected. The diffusion coefficients of the lithium ions in the positive and negative active materials, D_S^+ and D_S^-, respectively, have been obtained previously from impedance spectroscopy studies of half-cells. The active material in the positive electrode is assumed to be formed like spheres.[20,21] Thus, the lithium concentration in the positive material (c_S^+) is described by Fick's second law of diffusion in spherical coordinates

$$\frac{\partial c_S^+}{\partial t}r^2 = \frac{\partial}{\partial r}\left(r^2 D_S^+ \frac{\partial c_S^+}{\partial r}\right) \quad [4]$$

The lithium-ion transport in the active material of the negative electrode is treated in the same way as that of the positive electrode, except that the particles of the active material are modeled as flakes. This is consistent with the scanning electron microscopy (SEM) images of the material.[20,21,37] The lithium concentration in the active material (c_S^-) is thus described by Fick's second law of diffusion in Cartesian coordinates

$$\frac{\partial c_S^-}{\partial t} = \frac{\partial}{\partial z}\left(D_S^- \frac{\partial c_S^-}{\partial z}\right) \quad [5]$$

In the electrolyte, the lithium ions and the anions are transported by both diffusion and migration. Nyman et al.[23] have characterized the mass transport in the electrolyte [LiPF$_6$ dissolved in EC and EMC (3:7)] previously with the Maxwell–Stefan equation as a starting point, and the same theory and parameters are used in this work. In contrast to the Nernst–Planck equations that are often used in mass transport modeling, the Maxwell–Stefan equation takes into account interactions between ions and nonidealities in the electrolyte. These effects are important for electrolytes that have a high salt concentration. The lithium-ion concentration in the electrolyte (c_L) is described by Eq. 6 where the time derivate of the salt concentration is calculated from the space derivate of the anion flux

$$\varepsilon_L\frac{\partial c_L}{\partial t} = \frac{\partial}{\partial x}\left[(1 - c_L V_m^{LiPF_6})(\varepsilon_L)^{\beta_L} D_L\left(1 + \frac{\partial \ln f_\pm}{\partial \ln c_L}\right)\frac{c_{L,tot}}{c_{solv}}\frac{\partial c_L}{\partial x}\right]$$
$$+ \frac{\partial}{\partial x}\left[(1 - c_L V_m^{LiPF_6})(1 - t_{solv}^{Li^+})\frac{j_L}{F}\right] \quad [6]$$

In Eq. 6, ε_L is the volume fraction of the electrolyte in a battery domain, β_L is Bruggeman's constant for the electrolyte filled pores, $V_m^{LiPF_6}$ is the molar volume of the electrolyte salt (LiPF$_6$), D_L is the diffusion coefficient of the electrolyte salt with respect to the thermodynamic driving force, $1 + \partial \ln f_\pm/\partial \ln c_L$ is the thermodynamic enhancement factor, $c_{L,tot}$ is the total concentration of charged species, c_{solv} is the concentration of the solvent, $t_{solv}^{Li^+}$ is the transport number with respect to the solvent, j_L is the current density in the electrolyte, and F is Faraday's constant. D_L, $t_{solv}^{Li^+}$, and $1 + \partial \ln f_\pm/\partial \ln c_L$ are set as concentration-dependent according to Nyman et al.[23] The fluxes of the ions and the solvents are dependent on each other because a local volume deviation due to a change in salt concentration introduces a solvent flux to compensate for the change. The movements of the solvents are incorporated in the expression for the anion flux by setting the volume average velocity to zero.

The potential distribution in the electrolyte (φ_L) is also calculated from an expression derived from the Maxwell–Stefan equations

$$j_L = \kappa(\varepsilon_L)^{\beta_L}\left[-\frac{\partial \varphi_L}{\partial x} + \frac{2RT}{c_L F}(1 - t_+^0)\left(1 + \frac{\partial \ln f_\pm}{\partial \ln c_L}\right)\frac{\partial c_L}{\partial x}\right] \quad [7]$$

where κ is the ionic conductivity and is concentration-dependent, as described by Nyman et al.[23]

The solid and electrolyte phases are connected by the conservation of charge.[10] The current density in the electrolyte is coupled to the local current per active material area and the flux of lithium ions over the interface between the active particle surface and the electrolyte (J_n) by

$$\frac{\partial j_L}{\partial x} = aj_{loc} = aFJ_n \quad [8]$$

where a is the specific area of the active material particles in an electrode.

The local current per active material area is calculated using the Butler–Volmer equation

$$j_{loc} = c_S \cdot k_{a,0}\ \exp\left[\frac{\alpha_a F}{RT}\cdot(\varphi_S - \varphi_L - E_{ref})\right]$$
$$- c_L \cdot (c_{tot} - c_S) \cdot k_{c,0}\ \exp\left[-\frac{\alpha_c F}{RT}\cdot(\varphi_S - \varphi_L - E_{ref})\right] \quad [9]$$

where α_a and α_c are the transfer coefficients for the anodic and cathodic reactions in an electrode, R is the universal gas constant, T is the temperature, and $c_{S,tot}$ is the maximum concentration of lithium in the active material of an electrode. $k_{a,0}$ and $k_{c,0}$ are the reaction rate constants for the anodic and cathodic reactions, respectively, and are coupled by the following expression

$$k_{c,0} = k_{a,0} \cdot \frac{c_S}{c_L \cdot (c_{tot} - c_S)}\ \exp\left\{\frac{F}{RT}\cdot[E_{OCP}(c_S) - E_{ref}]\right\} \quad [10]$$

where E_{OCP} is the superficial open-circuit potential (OCP) of the active material and E_{ref} (also seen in Eq. 9) is an arbitrary value that is introduced to keep the anodic and cathodic reaction rate constants within a comparable order of magnitude. The reaction rate constants are obtained from Eq. 10 and measured values of the exchange current density. E_{OCP} for the active material in the positive and negative electrodes has been determined elsewhere.[20,21]

A contact resistance between the current collector and the porous matrix has also been reported.[38] The resistance is included in the model by subtracting the product of this contact resistance ($R_{contact}$) and the total current that is drawn from or added to the cell, the applied current density (j_{appl}) from the cell voltage.

The parameters in the model (Table I) are mainly obtained from separate studies of the electrodes in half-cells[19-21] and of the electrolyte.[23] Thus, the model is built in a bottom-to-top fashion. However, the contact resistance and the positive electrode's local resistance cannot be obtained in such a way. The stack pressure affects these parameters and consequently measuring these resistances in cells other than the 18650 cells would give false values. To determine the values of these parameters, an optimization procedure was performed. The simulated cell voltage curves were fitted to experimental cell voltage curves by connecting the COMSOL Multiphysics program with an optimization algorithm in MATLAB. The working principle of a similar optimization program has been reported earlier.[23] The two parameters do not markedly affect the cell voltage during the OCP periods and the two parameters each influence the voltage differently during periods of charge/discharge. Obtaining these two remaining values with an optimization procedure was therefore considered suitable. To further increase the accuracy in the values of the two resistances, the simulated cell voltage curves were fitted to the corresponding experimental cell voltage curves at both SOC 40 and 80 simultaneously. The local and contact resistances are considered independent of SOC because the solid phase concentration of lithium is assumed not to affect these resistances.[20]

The impact of not taking into account nonidealities, ion–ion interactions, and solvent movement in the electrolyte was studied by exchanging Eq. 6 and 7 with another set of equations based on the Nernst–Planck equation.[10] The electrolyte potential (Eq. 11) and concentration (Eq. 12) are then described by

$$j_L = (\varepsilon_L)^{\beta_L} F \left(-c_L F \frac{D_L^{Li^+} + D_L^{PF_6^-}}{RT} \frac{\partial \varphi_L}{\partial x} + 2D_L^{PF_6^-} \frac{\partial c_L}{\partial x} \right) \quad [11]$$

$$\varepsilon_L \frac{\partial c_L}{\partial t} = \frac{2D_L^{Li^+} D_L^{PF_6^-}}{D_L^{Li^+} + D_L^{PF_6^-}} (\varepsilon_L)^{\beta_L} \frac{\partial^2 c_L}{\partial x^2} + \frac{D_L^{PF_6^-}}{D_L^{Li^+} + D_L^{PF_6^-}} \frac{a j_{loc}}{F} \quad [12]$$

The diffusion coefficients for the lithium ion and hexafluorophosphate ion (the anion), denoted as $D_L^{Li^+}$ and $D_L^{PF_6^-}$ in Eq. 11 and 12, were calculated so that the effective diffusion coefficient and transport numbers in the Nernst–Planck equations would be the same as the ones in Eq. 6 and 7.

Data Analysis

A strategy for analyzing the data from the battery model was set up. The strategy is based on studying and quantifying the different subprocesses in the cell in terms of their influence on the polarization. The polarization arises due to three groups of subprocesses:[1]

1. Activation of the electrochemical reactions.
2. Mass transport of species.
3. Inadequate contact between different phases and materials in the electrodes.

The part of the polarization that is associated with the activation of the electrochemical reactions is called the activation overpotential in this study. Polarization due to mass transport arises due to two processes. The first one is due to the concentration gradients that are built up in the electrolyte and in the solid phase. In this work, this is called the diffusion polarization. The second one is the polarization that stems from the insufficient ionic conductivity in the electrolyte and the insufficient electronic conductivity in the solid phase. These are called ohmic potential drops. The third subprocess occurs both between the current collector and the porous matrix, and between the active and conductive materials in the positive electrode. The polarization due to the former effect is denoted as contact resistance
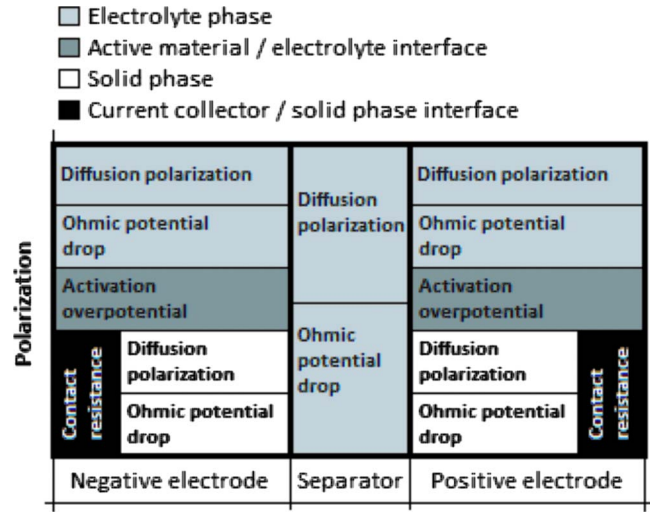

Figure 2. (Color online) The subprocess related polarizations within a lithium-ion battery cell.

and is modeled as a resistance. The latter effect is included in the activation overpotential of the positive electrode. In Fig. 2, a summary of the polarizations and where they appear is presented.

In a battery cell with planar electrodes, the polarization can easily be split up into parts that are associated with a subprocess. In contrast, for porous electrodes the electrochemical reaction is spread out in the electrode so that the total polarization is minimized. The electrochemical reaction therefore occurs at different conditions within the electrode and, thus, the polarization that is associated with, e.g., the activation of the electrochemical reaction, varies in the electrode. Yet, an expression for the average value for the polarization due to a subprocess (i) in a battery domain (an electrode or the separator) ($\eta_{ave,i}$) can be formulated

$$\eta_{ave,i} = \sum_{\substack{x_0=0 \\ n\to\infty}}^{x_n=L} \frac{I_{loc,i}(x)}{I_{tot}} \eta_{loc,i}(x) \quad [13]$$

In Eq. 13, the cell is split up into an infinite number of slices, where I_{loc} is the current that gives rise to the polarization (η_{loc}) in a slice. I_{tot} is the total current through the cell. L is the thickness of the electrodes or the separator. The average polarization is thus calculated from a weighted mean of the local polarizations.

For polarizations that occur on the electrolyte/electrode interface, Eq. 13 can be simplified to

$$\eta_{ave,i} = \int_0^L \frac{j_{loc}(x)}{j_{tot}} \cdot a\eta_{loc,i}(x)dx \quad [14]$$

where j_{tot} is the total current per cross-sectional area.

For polarizations that occur in the electrolyte or in the solid phase, Eq. 13 can be simplified to

$$\eta_{ave,i} = -\int_0^L \frac{j_\nu(x)}{j_{tot}} \cdot \frac{\partial \varphi_\nu(x)}{\partial x}dx \quad [15]$$

where φ_ν is the local electrochemical potential and j_ν is the local current per cross-sectional area in the solid or electrolyte phase.

The expressions for the average polarizations are seen in Table II. An inherent property from the model formulation is that the sum of the averaged polarization is equal to the total polarization of the cell ($E^{cell} - E_{ave}^{cell}$, Eq. A-9). A complete derivation of this and further explanation can be found in the Appendix. Using this strategy to calculate the averaged values of the polarizations associated with the subprocesses displayed in Fig. 2 allows us to compare them with

Table II. Expressions for calculation of the average subprocess related polarization.

Diffusion polarization electrolyte	$-\dfrac{1}{j_{tot}}\int_0^L \dfrac{2RT}{c_L F}\kappa_c \dfrac{\partial c_L}{\partial x}j_L dx$
Diffusion polarization solid phase	$\dfrac{1}{j_{tot}}\int_0^L aj_{loc}(E_{surf}-E_{ave})dx$
Ohmic potential drop electrolyte	$\dfrac{1}{j_{tot}}\int_0^L \dfrac{j_L^2}{\kappa_{eff}}dx$
Ohmic potential drop solid phase	$\dfrac{1}{j_{tot}}\int_0^L \dfrac{j_S^2}{\sigma_{eff}}dx$
Activation overpotential	$\dfrac{1}{j_{tot}}\int_0^L aj_{loc}(\varphi_S-\varphi_L-E_{surf})dx$
Contact resistance	$j_{appl}\cdot R_{contact}$

Figure 3. Simulated, measured, and equilibrium cell voltage during the EU-CAR cycle at SOC 40.

each other and to determine for which conditions a subprocess is responsible for increased polarization in the cell. With this procedure, all the irreversible losses during the cycle can be accounted for during the passage of current, whereas the periods of zero current do not contribute.

Experimental

Experiments were performed on fresh cylindrical 18650-type lithium-ion batteries designed for HEV use with a total capacity of 0.9 Ah each. The batteries were kindly supplied by Quallion LLC. The active materials were $LiNi_{0.8}Co_{0.15}Al_{0.05}O_2$ at the positive electrode and artificial graphite (MAG-10) at the negative electrode. As the electrolyte, 1.2 M $LiPF_6$ in EC:EMC (3:7 by weight) was used with a Celgard three-layer separator.[39] Details about the battery components and materials are presented in Table III.

To ensure careful temperature control, the battery was kept in an oil bath (Julabo F18) with a thermostat (Julabo VC). The battery cells were cycled according to a power-assist hybrid cycle according to EUCAR[24] at 25°C. The experiments were performed at both SOC 40 and 80.

For the experiments, a potentiostat (IM6, Zahner Elektrik) with a power booster (PP200, Zahner Elektrik) was used together with commercial software, Thales (Zahner Elektrik).

Results and Discussion

The work presented in this paper involved two steps. First, a mathematical model was developed and validated using experimental data from a battery cell. Second, model simulations were used to analyze the contributions to the total polarization from the different subprocesses and domains. This was done as snapshots in time and as an average over an entire HPPC test cycle.

The simulated cell voltage, together with the experimental data from EUCAR cycling of the 18650 cell, is shown in Fig. 3. The cycle was simulated using the optimized values of the local and contact resistances (see Table I). The fit between the measured and simulated cell voltages is excellent for the first and fourth galvanostatic polarization periods. A very good fit is also seen when the
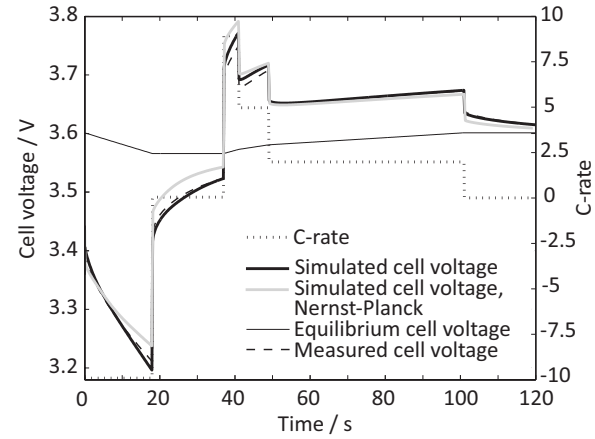
current is switched off. For the second and third polarization periods, there is a small difference between the measured and simulated values. Similar results were achieved for SOC 80. The polarization of the positive electrode around SOC 60 has been previously studied by Dees et al.[14] and the polarization of the positive electrode at SOC 40 and 80 is in the same order as in their study.

In the development of the model, several other versions of the model were also tested and compared to the experimental data to determine the necessary extent of details and some valuable conclusions were drawn. For example, the equations describing the mass transport in the electrolyte (Eq. 6 and 7) were exchanged with the Nernst–Planck equations (Eq. 11 and 12) that neglect the nonidealities and the ion–ion interactions of the electrolyte. For this case the simulated cell voltage, seen in Fig. 3, could not be optimized to fit the experiments satisfactorily. The influence of concentration-dependent transport properties (Eq. 6 and 7) was also investigated. No effect could be seen in the cell voltage when the transport properties were described with constants instead of functions depending on the salt concentration. A slight change in the concentration profiles could however be seen at high concentrations and, thus, concentration dependence was incorporated in the model. A model with a capacitative double layer at the interface between the active material particles and the electrolyte was also tested.

Simulations showed no significant double layer effect on the polarization of the cell for the galvanostatic charging and discharging procedures studied in this paper and it was therefore excluded from the final model. In the optimization of the model to the experimental data with the local and contact resistances as optimization parameters, the contact resistance had no effect upon the cell voltage when the current was switched off and the effect of the local resistance was minor during the same period. Thus, the good fit during that period further confirms the accuracy of the equations and parameters that describe the cell voltage.

Table III. Cell chemistry (battery manufacturer data).

|	
Negative	92 wt % MAG-10 graphite, 8 wt % PVDF binder
	5 mg cm^{-2} active loading density
	Porous electrode thickness (L^+) 35×10^{-6} m
Positive	84 wt % $LiNi_{0.8}Co_{0.15}Al_{0.05}O_2$, 8 wt % poly(vinylidene fluoride) (PVDF) binder, 4 wt % SFG-6 graphite, 4 wt % carbon black
	8 mg cm^{-2} active loading density
	Porous electrode thickness (L^-) 35×10^{-6} m
Separator	Celgard, 2325 polypropylene/polyethylene/polypropylene (PP/PE/PP)
	Separator thickness (L^S) 25×10^{-6} m
Electrolyte	1.2 M $LiPF_6$
	EC:EMC (3:7 by weight)
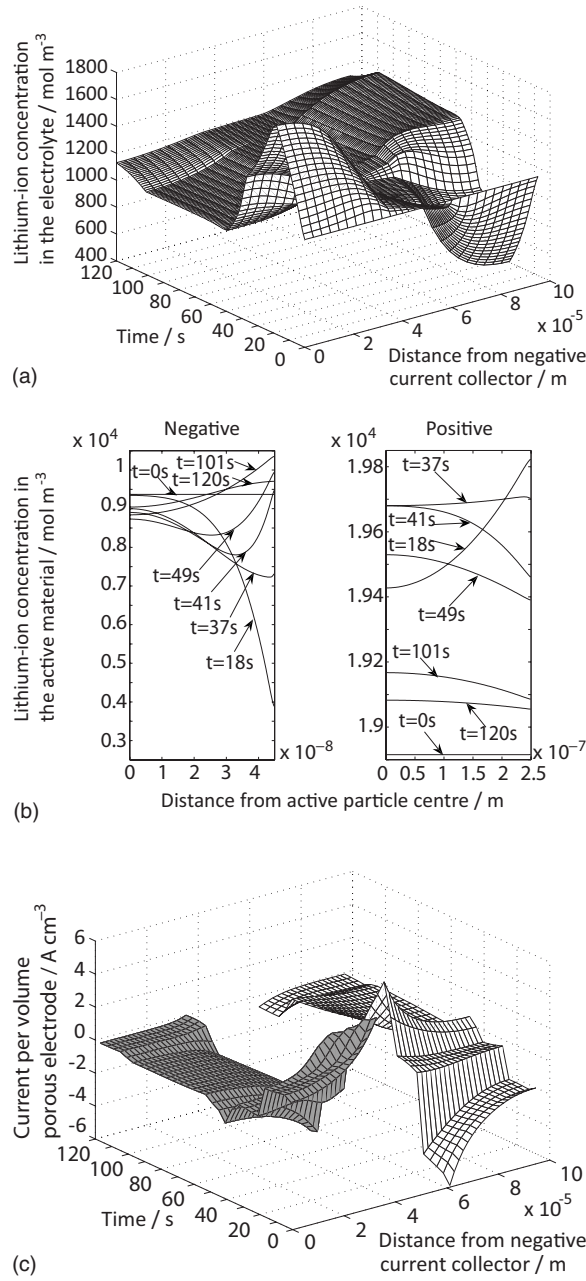
Figure 4. For EUCAR cycling at SOC 40: (a) Lithium-ion concentration in the electrolyte, (b) lithium-ion concentration in the active material of the porous electrodes at a point one-third of the electrode length from the separator, and (c) local current per volume porous electrode.

The spatial variation in the lithium-ion concentration, electrochemical potential, and reaction rates with time constitute the basis for the analysis of the polarization. Figure 4a-c shows a selection of the inner variables from the same simulation as in Fig. 3. The lithium-ion concentration in the electrolyte is displayed in Fig. 4a, the lithium concentration profiles in particles of the active material in Fig. 4b, and the distribution of the local current density along the depth of the porous electrodes in Fig. 4c.

For a single ion conductor or in the absence of mass transport limitations, the electrolyte concentration profile would be horizontal over the cell. However, because the electrolyte current is only partly carried by the lithium ion and mass transport is hindered, transport takes place due to both migration and diffusion. Thus, the concentration varies locally and this can be seen in Fig. 4a. During the periods of nonzero current, the concentration profiles build up, con-

tributing to the increasing polarization seen in Fig. 3. Conversely, when the current is switched off, both the concentration profiles and the cell voltage relax toward equilibrium.

A similar process takes place in the active material. Figure 4b shows distributions of lithium-ion concentration in an active material particle at a point one-third of the electrode length from the separator for seven different times during the cycle. Simulations are shown for both electrodes. Although the concentration differences are relatively small within the positive electrode particle, the differences are considerably larger within the negative electrode. This indicates that the negative electrode is more limited by solid phase diffusion. The behavior can be traced back to the particle diameter and the diffusion coefficient of the active material, and from these parameters the time constant for diffusion is calculated to be approximately 5 times higher for the negative particle.[3]

The local current density displays an uneven distribution along the depth of the electrodes, as seen in Fig. 4c. This is particularly pronounced in the positive electrode and during the initial discharge period. The uneven current distribution indicates that there exist electrolyte mass transport limitations. The figure gives no direct indication as to whether this is due to ohmic potential drop or diffusion polarization. However, the quick buildup of concentration gradients in Fig. 4a points out the diffusion polarization as important.

Although the results in Fig. 4a-c give interesting indications about limitations and irreversible energy losses, a quantification of the polarization and its contributing components requires further analysis. The method for analyzing the model data, as described in the Data Analysis section, is a new and important step in this direction. It enables the calculation of the contribution of each subprocess to the total polarization in the form of the average polarization of that process in a domain ($\eta_{ave,i}$). Further, to analyze the contribution to polarization over a whole HPPC cycle, a cycle-averaged polarization was defined according to Eq. 13. The cycle-averaged polarization is calculated as a rate of irreversible energy loss due to the subprocess in question, integrated over time and normalized with the total amount of charge passed during the cycle.

$$\eta_{ave,i}^{cycle} = \frac{1}{\int_0^{t_{cycle}}|j_{tot}|dt}\int_0^{t_{cycle}}\eta_{ave,i}j_{tot}dt \qquad [16]$$

where t_{cycle} is the total time for an HPPC cycle.

The simulation of an EUCAR cycle at SOC 40, as shown in Fig. 3 and 4, was analyzed using this approach. In Fig. 5a, the relative contributions to the cycle-averaged polarization are displayed.

The contact resistance and the ohmic potential drop in the electrolyte are responsible for the larger part of the polarization over the cycle. The diffusion polarization in the electrolyte and the solid phase and the activation overpotential are smaller yet significant. If the ohmic potential drop is added to the electrolyte diffusion polarization, the importance of the mass transport to the cell performance is clear as it amounts to 43% of the total polarization. The effect of the ohmic potential drop in the solid phase is negligible in this cell. The cycle-averaged polarization is closely connected to the energy efficiency for a charge-neutral cycle (ε_W)

$$\varepsilon_W = 1 - \frac{\eta_{ave,tot}^{cycle} \cdot \int_0^{t_{cycle}}|j_{tot}|dt}{W_{charge}} \qquad [17]$$

where W_{charge} is the amount of energy that is required for the charging and $\eta_{ave,total}^{cycle}$ is the total cycle-averaged polarization in the cell. The energy efficiency of the battery was 89.0% at SOC 40 and 91.5% at SOC 80. The difference between the two SOCs arises mainly in the solid phase of the electrodes because the diffusion polarization in the solid phase is considerably lower at SOC 80 (7% of the total polarization).

To investigate the location of the polarization, in addition to the nature of it, it was divided among the three domains: the positive and negative electrodes and the separator. The relative contributions are shown in Fig. 5b. Most of the polarization occurs within the electrodes. The negative electrode contributes slightly more than the
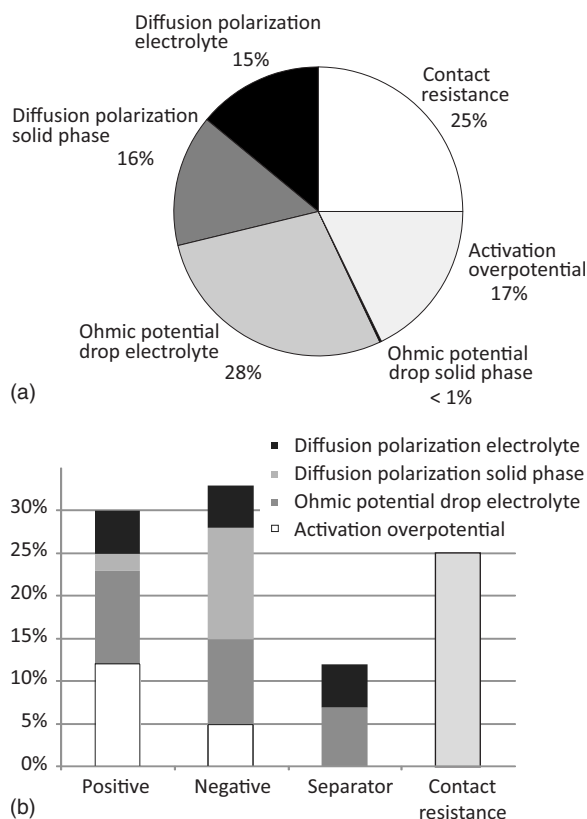
(a)

(b)

Figure 5. (a) Distribution of cycle-averaged polarization and (b) the contribution of each battery domain to the polarization for an EUCAR cycle at SOC 40.

positive, 33 and 30%, respectively. The diffusion polarization in the solid phase is more important in the negative electrode, which is in line with the indications of Fig. 4b, whereas the positive electrode is considerably more polarized by the activation overpotential. The positive electrode is slightly more polarized by the subprocesses in the electrolyte than the negative electrode, which is more polarized by the subprocesses occurring in the solid phase and the active material/electrolyte interface.

The variation over time for the polarization from each of the six subprocesses is displayed in Fig. 6. Initially, the polarization is dominated by the contact resistance, the ohmic potential drop, and the activation overpotential. The contact resistance is constant for a
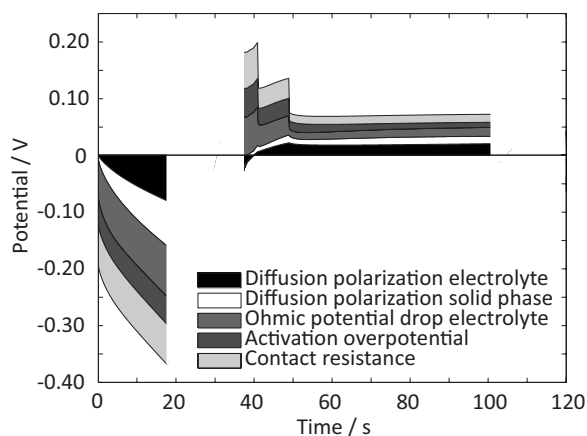

Figure 6. Contributing polarizations in the battery cell during the EUCAR cycle at SOC 40.
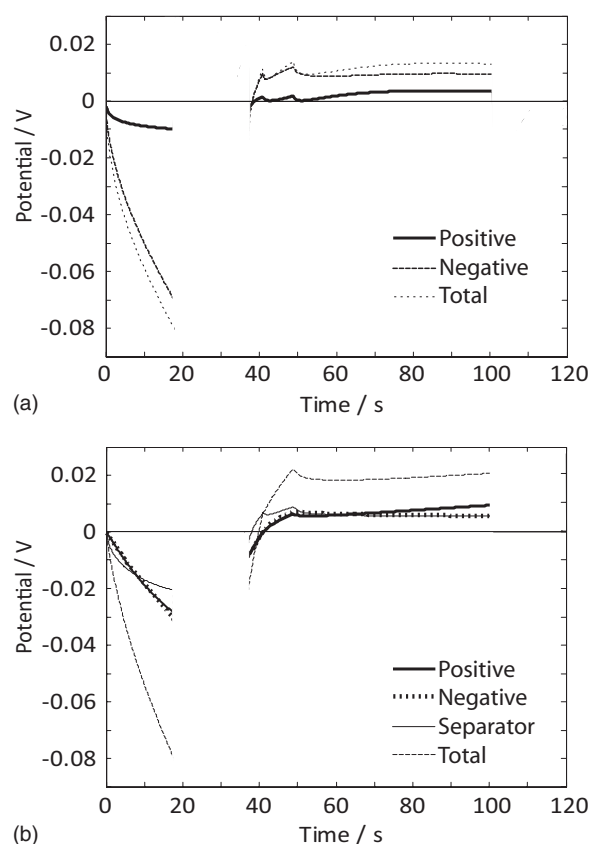

(a)

(b)

Figure 7. Diffusion polarization in the (a) solid phase and (b) electrolyte during the EUCAR cycle at SOC 40.

given current, whereas the ohmic potential drop increases slightly with time during each current step as the reaction zone moves deeper into the electrodes toward the current collector. The activation overpotential is more or less constant with time during each current step. Conversely, the two diffusion polarizations show large variation with time. For example, during the 18 s of discharge at 10C rate, their contribution grows from 0 to more than 40%, which is due to the buildup of significant concentration gradients in the active material and the electrolyte. When the charge at 9C rate begins at 37 s into the cycle, the diffusion polarizations actually contribute to a decrease in the cell polarization during a couple of seconds. This can be understood by considering that the concentration profiles created by the discharge pulse have not had time to relax completely, and the nonuniformities actually favor the charge process. Figure 7a and b presents a separation of the diffusion polarizations among the three domains of the cell. The contribution to a decrease in the polarization is seen in both phases in the domains. As displayed in Fig. 7a, the increase in the diffusion polarization in the solid phase is mainly attributed to the negative electrode (cf. Fig. 4b and 5b). Conversely, Fig. 7b shows that the diffusion polarization in the electrolyte is evenly distributed among the three domains (cf. Fig. 5b).

The contributions of the subprocesses to the total polarization change if the cell design is altered. To give an example of how the cycle-averaged polarization concept can be used to study the relationship between the design of the cell and the processes within it, two design parameters were varied. First, the thickness of the electrodes was doubled and, second, the lithium-ion concentration in the electrolyte was set to 500 mol m^{-3}. In Fig. 8a, the average polarization in a cell with double porous electrode thickness is shown. To compensate for the double amount of active material, the currents were set twice as high. This is shown in the contact resistance, whose contributing part to the polarization is doubled (cf. Fig. 6).
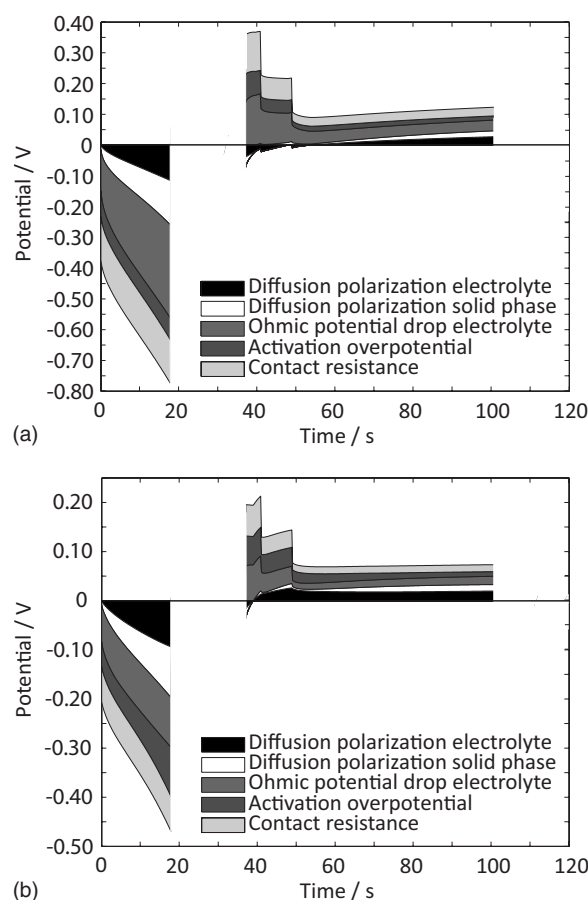
Figure 8. Contributing polarizations in a battery cell with (a) double porous electrode thickness (2*L*) and (b) an initial lithium-ion concentration in the electrolyte of 500 mol m⁻³ during the EUCAR cycle at SOC 40.

Figure 9. Simulated cell voltage for the (a) FreedomCAR and (b) ISO-energy test cycle at SOC 40.

The diffusion polarization in the electrolyte and the solid phase is also close to double, whereas the activation polarization remains largely unchanged. The ohmic potential drop in the electrolyte exhibits an especially high increase because the lithium ions need to be transported a longer distance in the electrolyte. The contributions of the diffusion polarizations to the decrease in total polarization are effective during a longer time than before because the diffusion length is longer. The increased polarization affects the energy efficiency, which drops to 79.3%.

Figure 8b shows the average polarizations when the lithium-ion concentration in the electrolyte is 500 mol m³. The activation overpotential is especially affected by the lower salt concentration. At the end of the 10C rate discharge, it increases rapidly. The increase is attributed to the positive electrode. As an average over the whole cycle, 15% of the total polarization originates from the activation overpotential in the positive electrode (cf. Fig. 5b). This can be explained by the fact that the initial lithium-ion concentration is not sufficient to supply the intercalation reaction, leading to a depletion of lithium ions close to the positive current collector. The lower salt concentration reduces the energy efficiency to 87.7%.

To investigate the influence of the load on the cell, a Freedom-CAR cycle[14] and an ISO (International Organization for Standardization)-energy cycle were simulated with the values given in Table I. The simulated voltage response of the current for the two HPPC test cycles is displayed in Fig. 9. The FreedomCAR cycle contains one charge and one discharge period separated by an open-circuit period (Fig. 9a). The ISO-energy cycle is charge-neutral just like the EUCAR cycle, but it is more complex and contains several charge and discharge periods separated by OCP periods (Fig. 9b).
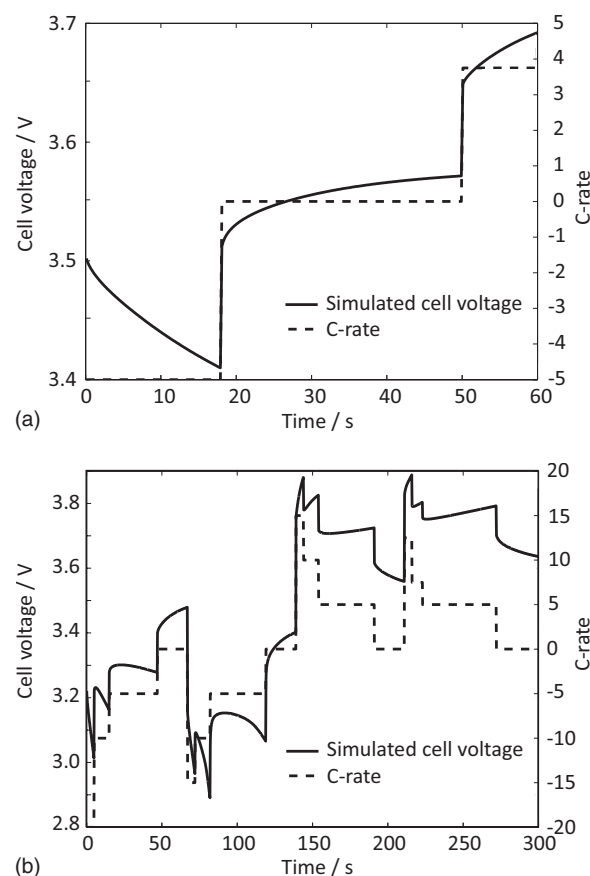
The ISO-energy cycle covers an SOC span (ΔSOC) of 20%, which indicates that it strains the cell more than the EUCAR cycle with a ΔSOC of 5%.

Figure 10 shows the origin of the cycle-averaged polarization for the three HPPC test cycles. Although the cycle-averaged polarization of the FreedomCAR and the EUCAR cycles are of different sizes, the breakdown of the polarization over the whole cell is almost the same. When looking at the battery domains, a difference
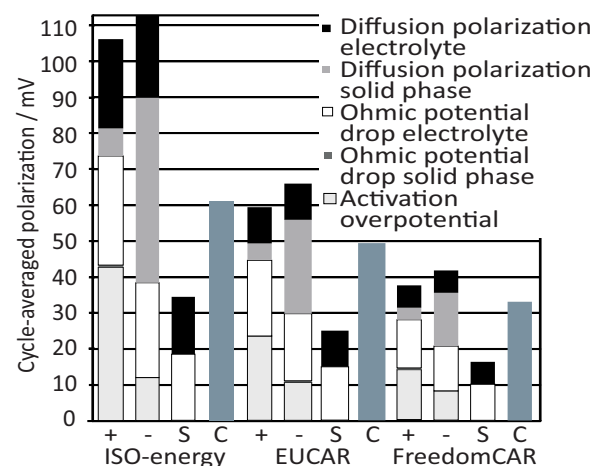

Figure 10. (Color online) Cycle-averaged polarizations for an EUCAR, a FreedomCAR, and an ISO-energy test cycle at SOC 40. +: Positive electrode, −: Negative electrode, S: Separator, and C: Contact resistance.

between the cycles is seen in the negative electrode; the EUCAR cycle has a higher diffusion polarization in the solid phase and lower activation overpotential than the FreedomCAR cycle. The diffusion polarization in the solid phase of the negative electrode becomes even more important for the ISO-energy cycle. For the three cycles, the mass transport in the electrolyte accounts for an equal share of the polarization. However, the fraction of the mass transport limitation related to diffusion polarization is more pronounced for the ISO-energy cycle. It is the longer periods of charge/discharge and higher C-rates that increase the diffusion polarization in the electrolyte and the solid phase of the negative electrode and it is explained by the significant concentration gradients that are built up. The energy efficiency of the ISO-energy test cycle is 83.4%, which is considerably lower than that for the EUCAR cycle. The energy efficiency could not be defined for the FreedomCAR cycle because it is not charge-neutral.

The use of this method of analysis opens up the possibility of determining the limiting features of a lithium-ion battery cell in an effective way. Not only does the method offer an understanding of what kind of subprocess constrains the battery performance but also where within the battery the limitations exist and when they occur. The presented method is a valuable tool for choosing optimal operational condition and design.

Results show that the limitations vary depending on how the battery is utilized. The design of the cell in this paper has already been optimized for high power applications but the parameter study shows an example of how the concept of average polarization can be used. As the study showed, a double electrode thickness gives a drop in performance. This is because the inner part of the electrodes cannot be sufficiently utilized due to mass transport limitations in the electrolyte. Optimizing performance through change in this battery design would therefore require improving electrolyte mass transport properties. This could involve decreasing the tortuosity, which is a key factor for transport in the porous structure of the electrodes and the separator. It can be achieved by changing the structure of the voids in the solid phase. If the tortuosity is lowered while keeping the electrolyte volume fraction in the electrodes low, a higher energy density can be achieved.

The process of quantifying the polarization could be further developed by separating the total contact resistance into positive and negative electrode parts. To retrieve the necessary parameters by experiments, a reference electrode introduced directly to the cell is required. The description of the solid phase diffusion may also be discussed as we have chosen to describe the size distribution of the particles by one averaged value. It has been suggested that describing the size distribution by several particle sizes would enhance the fit between the model and the experiment.[14] However, our model could, despite this assumption, describe the cell voltage correctly (see Fig. 3). Instead, to obtain good fits, it is more important to describe the electrolyte properties in detail.

Conclusions

A method based on a model that describes the physical and chemical processes occurring in a lithium-ion battery cell has been developed to investigate the polarization during an HPPC test cycle. The following main conclusions can be drawn from this study:

1. The mathematical model, based on well-founded physically based submodels, was able to simulate the cell voltage accurately even for high current loads (>5 C).

2. The polarization in a cell can be split up into parts associated with the activation of electrochemical reactions, mass transport, and inadequate contact between materials in either the electrodes or in the separator.

3. The method is a valuable tool for quantifying and localizing the processes that are responsible for the polarization.

The method was used to study the polarization of a battery cell with a $LiNi_{0.8}Co_{0.15}Al_{0.05}O_2|1.2$ M $LiPF_6$ in EC:EMC $(3:7)|MAG$-10 chemistry. It was concluded that

1. When the cell was pulsed according to EUCAR at SOC 40, the cycle-averaged polarization arose mainly in the porous electrodes. All subprocesses except for the ohmic potential drop in the solid phase contributed significantly to the polarization of the cell. The contact resistance and the ohmic potential drop in the electrolyte accounted together for more than half of the polarization over the cycle. When the polarization was studied as a snapshot in time, the increase in the polarization during a constant current load was mainly attributed to the increase in the diffusion polarizations.

2. In a design parameter study, the activation overpotential showed a tendency to increase rapidly during the initial discharge of the EUCAR cycle when the initial electrolyte concentration was lowered.

3. The diffusion polarization in the electrolyte and the solid phase of the negative electrode became more significant with cycles that contained high current loads during long times, such as the ISO-energy cycle.

Acknowledgments

Appendix

The summation of the average polarizations in a porous electrode gives the electrode polarization

$$E - E_{ave} = \frac{1}{j_{tot}}\left(\int_0^L a j_{loc}(\varphi_S - \varphi_L - E_{surf})dx + \int_0^L a j_{loc}(E_{surf} - E_{ave})dx + \int_0^L \frac{j_S^2}{\sigma_{eff}}dx \right.$$
$$\left. + \int_0^L \frac{j_L^2}{\kappa_{eff}}dx - \int_0^L j_L \cdot \frac{2RT}{c_L F}\kappa_c\frac{\partial c_L}{\partial x}dx \right) \qquad [A-1]$$

where E is the electrode potential and E_{ave} is the OCP of the active material after an infinite long time after current interruption and is calculated from the OCP expression.[6,8] E_{surf} is dependent on the concentration of lithium at the surface of the active material (c_{surf}) and it thus varies with the depth of the electrodes and with time. It is equal to the value of the OCP expression[20,21] when the concentration within the solid phase is c_{surf}. As the concentration of lithium at the surface of the active material relaxes to the equilibrium concentration, the value of E_{surf} relaxes to E_{ave}. σ_{eff} is the effective electronic conductivity, κ_{eff} is effective ionic conductivity, and κ_c is the concentration conductivity. j_{tot} is the total current density that is drawn from or added to the electrode and is calculated by

$$j_{tot} = \int_0^L a j_{loc}dx \qquad [A-2]$$

The left side of Eq. A-1 can be derived from the right side by rewriting the expressions for the average polarizations. The sum of the average polarizations for the potential drop in the electrolyte and the ohmic potential drop in the solid phase can be rewritten as

$$\int_{x_1}^{x_2} \left(\frac{j_S^2}{\sigma_{eff}} + \frac{j_L^2}{\kappa_{eff}} - j_L \cdot \frac{2RT}{c_L F} \kappa_c \frac{\partial c_L}{\partial x} \right) dx$$

$$= \int_{x_1}^{x_2} \left(-j_S \frac{\partial \varphi_S}{\partial x} - j_L \frac{\partial \varphi_L}{\partial x} \right) dx$$

$$= \int_{x_1}^{x_2} \left[-\frac{\partial (j_S \varphi_S)}{\partial x} + \varphi_S \underbrace{\frac{\partial j_S}{\partial x}}_{-aj_{loc}} - \frac{\partial (j_L \varphi_L)}{\partial x} + \varphi_L \underbrace{\frac{\partial j_L}{\partial x}}_{aj_{loc}} \right] dx$$

$$= \int_{x_1}^{x_2} -aj_{loc}(\varphi_S - \varphi_L) dx - \left(\underbrace{\frac{j_L}{\int_{x_1}^{x_2} aj_{loc} dx}}_{} \varphi_L \Big|_{x=x_2} - \underbrace{(j_S \varphi_S)|_{x=x_2}}_{=0} + \underbrace{(j_L \varphi_L)|_{x=x_1}}_{=0} \right)$$

$$+ \left(\underbrace{\frac{j_L}{\int_{x_1}^{x_2} aj_{loc} dx}}_{} \varphi_S \right) \Big|_{x=x_1}$$

$$= \int_{x_1}^{x_2} -aj_{loc}(\varphi_S - \varphi_L) dx + \int_{x_1}^{x_2} aj_{loc} dx \cdot (\varphi_S|_{x=x_1} - \varphi_L|_{x=x_2}) \qquad [\text{A-3}]$$

where x_1 and x_2 are the points for the interface between the current collector and the electrode and the interface between the electrode and the separator, respectively.

The sum of the average polarizations for the activation overpotential and the diffusion polarization in the solid can be rewritten as

$$\int_{x_1}^{x_2} aj_{loc}(\varphi_S - \varphi_L - E_{surf}) dx + \int_{x_1}^{x_2} aj_{loc}(E_{surf} - E_{ave}) dx$$

$$= \int_{x_1}^{x_2} aj_{loc}(\varphi_S - \varphi_L - E_{ave}) dx \qquad [\text{A-4}]$$

The left hand side of Eq. A-1 is obtained by taking the sum of Eq. A-3 and A-4

$$\int_{x_1}^{x_2} -aj_{loc}(\varphi_S - \varphi_L) dx + j_{tot}(\varphi_S|_{x=x_1} - \varphi_L|_{x=x_2}) + \int_{x_1}^{x_2} aj_{loc}(\varphi_S - \varphi_L - E_{ave}) dx$$

$$= -\int_{x_1}^{x_2} aj_{loc} E_{ave} dx + j_{tot}(\varphi_S|_{x=x_1} - \varphi_L|_{x=x_2}) \qquad [\text{A-5}]$$

where $\varphi_S|_{x=x_1} - \varphi_L|_{x=x_2}$ is equal to the potential of the porous electrode (E). This with Eq. A-2 simplifies Eq. A-5 into

$$-\int_{x_1}^{x_2} aj_{loc} E_{ave} dx + \int_{x_1}^{x_2} aj_{loc} dx \cdot (\varphi_S|_{x=x_1} - \varphi_L|_{x=x_2}) = (E - E_{ave}) \cdot j_{tot} \quad [\text{A-6}]$$

Equation A-6 verifies that Eq. A-1 applies and that the sum of the average polarizations is equal to the total polarization.

The total polarization in the cell is calculated by taking the sum of the polarizations in the porous electrode and the separator and by adding it to the voltage drop caused by the contact resistance. The polarization in the separator ($E^{\Delta s}$) is expressed as

$$E^{\Delta s} = \frac{1}{j_{appl}} \left[\int_0^{L^S} \left(\frac{j_L^2}{\kappa_{eff}} \right) dx - \int_0^{L^S} j_L \cdot \frac{2RT}{c_L F} \kappa_c \frac{\partial c_L}{\partial x} dx \right] \qquad [\text{A-7}]$$

The applied current density (j_{appl}) is defined as the total current density drawn from or added to the positive electrode and is calculated by

$$j_{appl} = \int_0^{L^+} a^+ j_{loc} dx \qquad [\text{A-8}]$$

Finally, the sum of all the polarizations in the cell is

$$E^{cell} - E_{ave}^{cell} = (E^+ - E_{ave}^+) - (E^- - E_{ave}^-) + E^{\Delta s} + j_{appl} \cdot R_{contact} \qquad [\text{A-9}]$$

The splitting procedure of the polarization can be compared to the separation of the generated heat in a battery cell as presented by Rao and Newman.[40]

List of Symbols

a	specific interfacial area, m^{-1}
c	concentration, $mol\ m^{-3}$
D_L	diffusion coefficient with respect to the thermodynamic driving force, $m^2\ s^1$
$D_L^{Li^+}, D_L^{PF_6}$	self-diffusion coefficient for Li^+ and PF_6^-, respectively, $m^2\ s^{-1}$
E	electrode potential, V
E_{cell}	battery cell potential, V
E_{OCP}	superficial OCP of the active material, V
$E^{\Delta s}$	polarization separator, V
F	Faraday's constant, 96,487 As mol^{-1}
I_{loc}	the current that give rise to the polarization, A
I_{tot}	the total current through the cell, A
j	current density, A m^{-2}
j_{appl}	applied current density (per cross-sectional area), defined in Eq. A-8, A m^{-2}
j_{loc}	local current per active material area, A m^{-2}
j_{tot}	total current per cross-sectional area, defined in Eq. A-2, A m^{-2}
J_n	pore-wall flux density across interface, $mol\ m^{-2}\ s^{-1}$
$k_{a,0}$	anodic reaction rate constant at equilibrium, $m^3\ s^{-1}$
$k_{c,0}$	cathodic reaction rate constant at equilibrium, $m^3\ s^{-1}$
L	length/thickness of battery component, m
r	radial distance in a spherical particle of active material, m
r_p^+	particle radius active material particle in the positive electrode, m
R	universal gas constant, 8.3143 J $mol^{-1}\ K^{-1}$
$R_{contact}$	contact resistance, $\Omega\ m^2$
R_{loc}^+	local resistance positive electrode, $\Omega\ m^2$
t_+^0	transport number of Li^+ with solvent as reference
t_{cycle}	length of HPPC test cycle, s
T	temperature, K
W_{charge}	energy loss per cross-sectional area during charging, J m^{-2}
x	distance in porous electrode, m
z	normal distance in a flake of active material, m
z_p^-	half thickness of flake-shaped active material particles negative electrode, m

Greek

α	transfer coefficient (anode, cathode)
β	Bruggeman's constant
ε	volume fraction of the electrolyte
ε_W	energy efficiency
η_{ave}	polarization averaged over a battery domain, V
η_{local}	local polarization, V
κ	ionic conductivity of the electrolyte phase, S m^{-1}
κ_c	concentration conductivity $(1 + t_+^0) \cdot (1 + \partial\ \ln\ f_{\pm}/\partial\ \ln\ c_L)$
ν	phase
σ	electronic conductivity, S m^{-1}
φ	electric potential, V

Subscripts

cS	electronic conductive solid phase
cycle	for a cycle
eff	effective parameter (accounting for the porosity and tortuosity of a porous electrode)
i	subprocess
L	liquid (electrolyte) phase
p	active particle
ref	reference
S	active material solid phase
tot	total

Superscripts

+	positive electrode
−	negative electrode
cell	cell
s	separator

References

1. C. H. Hamann, A. Hamnet, and W. Vielstich, *Electrochemistry*, 2nd ed., Wiley-VCH, Weinheim, Germany (2007).
2. M. Doyle, T. F. Fuller, and J. Newman, *J. Electrochem. Soc.*, **140**, 1526 (1993).
3. T. F. Fuller, M. Doyle, and J. Newman, *J. Electrochem. Soc.*, **141**, 1 (1994).
4. T. F. Fuller, M. Doyle, and J. Newman, *J. Electrochem. Soc.*, **141**, 982 (1994).
5. M. Doyle and J. Newman, *Electrochim. Acta*, **40**, 2191 (1995).
6. M. Doyle, J. Newman, A. S. Gozdz, C. N. Schmutz, and J. M. Tarascon, *J. Electrochem. Soc.*, **143**, 1890 (1996).
7. S. Atlung, K. West, and T. Jacobsen, *J. Electrochem. Soc.*, **126**, 1311 (1979).
8. K. West, T. Jacobsen, and S. Atlung, *J. Electrochem. Soc.*, **129**, 1480 (1982).
9. S. Atlung, B. Zachauchristiansen, K. West, and T. Jacobsen, *J. Electrochem. Soc.*, **131**, 1200 (1984).
10. J. Newman and K. Thomas-Alyea, *Electrochemical Systems*, 3rd ed., Wiley-Interscience, New Jersey (2004).
11. L. Nylen, M. Behm, A. Cornell, and G. Lindbergh, *Electrochim. Acta*, **52**, 4513 (2007).
12. E. Nilsson, J. Berendson, and E. Fontes, *Bioelectrochem. Bioenerg.*, **47**, 11 (1998).
13. F. Jaouen and G. Lindbergh, *J. Electrochem. Soc.*, **150**, A1699 (2003).
14. D. Dees, E. Gunen, D. Abraham, A. Jansen, and J. Prakash, *J. Electrochem. Soc.*,

155, A603 (2008).

15. S. G. Stewart, V. Srinivasan, and J. Newman, *J. Electrochem. Soc.*, **155**, A664 (2008).
16. P. Albertus, J. Couts, V. Srinivasan, and J. Newman, *J. Power Sources*, **183**, 771 (2008).
17. R. Darling and J. Newman, *J. Electrochem. Soc.*, **144**, 4201 (1997).
18. V. Srinivasan and J. Newman, *J. Electrochem. Soc.*, **151**, A1517 (2004).
19. N. Mellgren, S. Brown, M. Vynnycky, and G. Lindbergh, *J. Electrochem. Soc.*, **155**, A304 (2008).
20. S. Brown, N. Mellgren, M. Vynnycky, and G. Lindbergh, *J. Electrochem. Soc.*, **155**, A320 (2008).
21. S. Brown, Ph.D. Thesis, KTH, Stockholm (2008).
22. P. Georen and G. Lindbergh, *Electrochim. Acta*, **49**, 3497 (2004).
23. A. Nyman, M. Behm, and G. Lindbergh, *Electrochim. Acta*, **53**, 6356 (2008).
24. EUCAR, Traction Battery Working Group, Specification of Test Procedures for Hybrid Electric Vehicle Traction Batteries (1998).
25. P. Arora, R. E. White, and M. Doyle, *J. Electrochem. Soc.*, **145**, 3647 (1998).
26. F. Lantelme, A. Mantoux, H. Groult, and D. Lincot, *Electrochim. Acta*, **47**, 3927 (2002).
27. Z. Mao and R. E. White, *J. Power Sources*, **43**, 181 (1993).
28. G. S. Nagarajan, J. W. Van Zee, and R. M. Spotnitz, *J. Electrochem. Soc.*, **145**, 771 (1998).
29. K. Smith and C. Y. Wang, *J. Power Sources*, **161**, 628 (2006).
30. K. E. Thomas, S. E. Sloop, J. B. Kerr, and J. Newman, *J. Power Sources*, **89**, 132 (2000).
31. M. W. Verbrugge, D. R. Baker, and B. J. Koch, *J. Power Sources*, **110**, 295 (2002).
32. M. W. Verbrugge and B. J. Koch, *J. Electrochem. Soc.*, **150**, A374 (2003).
33. C. Fellner and J. Newman, *J. Power Sources*, **85**, 229 (2000).
34. *Advances in Lithium-Ion Batteries*, 1st ed., W. A. van Schalkwijk and B. Scrosati, Editors, Kluwer Academic/Plenum Publishers, New York (2002).
35. D. Dees, E. Gunen, D. Abraham, A. Jansen, and J. Prakash, *J. Electrochem. Soc.*, **152**, A1409 (2005).
36. P. Albertus, J. Christensen, and J. Newman, *J. Electrochem. Soc.*, **156**, A606 (2009).
37. M. Herstedt, D. P. Abraham, J. B. Kerr, and K. Edstrom, *Electrochim. Acta*, **49**, 5097 (2004).
38. M. Doyle and Y. Fuentes, *J. Electrochem. Soc.*, **150**, A706 (2003).
39. R. Elger, Licentiate Thesis, KTH, Stockholm (2004).
40. L. Rao and J. Newman, *J. Electrochem. Soc.*, **144**, 2697 (1997).
41. K. K. Patel, J. M. Paulsen, and J. Desilvestro, *J. Power Sources*, **122**, 144 (2003).
42. P. Arora and Z. M. Zhang, *Chem. Rev. (Washington, D.C.)*, **104**, 4419 (2004).